Journal of Applied Geophysics 160 (2019) 171–182

Contents lists available at ScienceDirect

Journal of Applied Geophysics

journal homepage: www.elsevier.com/locate/jappgeo

3D MT modeling using the T–Ω method in general anisotropic media

Tiaojie Xiao [a,b,*], Xiangyu Huang [c], Yun Wang [b]

[a] Institute of Geochemistry, Chinese Academy of Sciences, Guiyang 550002, China
[b] University of Chinese Academy of Sciences, Beijing 100049, China
[c] School of Geosciences and Info-Physics, Central South University, Changsha 410083, China

ARTICLE INFO

Article history:
Received 16 May 2018
Received in revised form 15 November 2018
Accepted 17 November 2018
Available online 24 November 2018

Keywords:
Magnetotelluric
Anisotropy
Three-dimensional
Modeling
Finite element method

ABSTRACT

We developed an algorithm to simulate magnetotelluric responses for three-dimensional general electrical anisotropic structures with finite element (FE) method. From the Maxwell's equations, the curl-curl equation in terms of the electric vector potential and the magnetic scalar potential is obtained by decomposing the magnetic field into the incident field and the resultant field. For this method, the only unknown variable in the air is the magnetic scalar potential. Galerkin weighted residual method is adopted to generate the variational equations. Then we made a comparison with the edge-based FE method which is in terms of electric fields to validate the accuracy of this method. Later, two types of anisotropic models are studied and the results are analyzed in detail. Finally, based on these analyses, two main meaningful conclusions are obtained.

© 2018 Elsevier B.V. All rights reserved.

1. Introduction

Magnetotelluric (MT) modeling in electrical anisotropic media has been a hot topic for a long time (O'Brien and Morrison, 1967; Dekker and Hastie, 1980; Yin, 2003; Li and Pek, 2008; Jones, 2012; Hu et al., 2013; Ben, 2016; Xiao et al., 2018). The preferred orientation within crystals and the inability to resolve ordered inhomogeneity caused the electric anisotropy in microscopic scale and macroscopic scale, respectively (Kong et al., 2018). The electrical anisotropy in the earth cannot be ignored, otherwise it would probably bring misinterpretation even errors for MT data interpretation (Linde and Pedersen, 2004; Häuserer and Junge, 2011). Therefore it is necessary and significant to study the MT responses in electrical anisotropic media.

The electrical anisotropy usually is defined by three principal conductivities and three Euler's angles, and two defining methods are available (Yin, 2000; Pek and Santos, 2002). For MT modeling in one-dimensional (1D) and two-dimensional (2D) anisotropic media, many studies have been done (Reddy and Rankin, 1971; Yin, 2000; Li, 2002; Li and Pek, 2008; Xue and Ji, 2018). For 1D anisotropic earth models, it has analytical solutions (Pek and Verner, 1997); however, there is inherent non-uniqueness in 1D inversion as some anisotropic parameters cannot be uniquely resolved for some certain layered anisotropic models (Yin, 2003). In 2D electrical anisotropic media, the electric field and the magnetic field must be solved simultaneously as they are inseparable (Li, 2002). The finite-element (FE) method, the finite-difference (FD) method, and the integral equation (IE) method are the three commonly used methods to simulate electromagnetic (EM) responses (Everett, 2012; Cai et al., 2014). For three-dimensional (3D) electric anisotropic structures, based on the staggered-grid FD method which automatically satisfies the energy conservation law, Weidelt et al. (1999) implemented a FD algorithm to simulate MT responses in 3D anisotropic media; based on the nodal FE method, Li (2000) developed an algorithm using the nodal FE method, however this method has two main disadvantages, namely it neither can meet the divergence condition nor is able to simulate the mutation of the electric field at electric discontinuous interfaces; therefore, Xiao et al. (2018) implemented the edge-based FE method which avoided these disadvantages of the node-based FE method, however it is hexahedral element adopted to discretize the study domain which is not suitable for topography and irregular anomalies; Liu et al. (2018) developed the adaptive FE method for 3D MT modeling in anisotropic media, which is convenient to irregular anomalies and topography; however, to the author's knowledge there is no published papers which use the IE method to simulate MT responses in 3D anisotropic media. Besides, there is a paper available for MT inversion though it is for 3D axial anisotropic media (Cao et al., 2018).

Most EM forward modeling methods are in terms of the electric fields or the magnetic fields (Tan et al., 2003; Ren et al., 2013; Li et al., 2016; Wang et al., 2016; Kong et al., 2018). Besides, there are some other methods which are in terms of EM potentials. In addition, most of these methods are $\mathbf{A}-\phi$ methods, where $\mathbf{A}$ is the magnetic vector potential and ϕ is the electrical scalar potential (Haber et al., 2000; Badea et al., 2001; Puzyrev et al., 2013; Cai, 2015; Chen et al., 2017). Besides $\mathbf{A}-\phi$ method, $\mathbf{T}-\Omega$ method which was originally presented

* Corresponding author at: Institute of Geochemistry, Chinese Academy of Sciences, Guiyang 550002, China.
E-mail address: 'xiaotiaojie16@mails.ucas.ac.cn' (T. Xiao).

https://doi.org/10.1016/j.jappgeo.2018.11.012
0926-9851/© 2018 Elsevier B.V. All rights reserved.

by Bíró (1999) also can be used to simulate MT responses where **T** is the electric vector potential and Ω is the magnetic scalar potential (Mitsuhata and Uchida, 2004). Comparing to **A** − ϕ method, this method has two advantages. On the one hand, the magnetic scalar potential is the only unknown variable in the air zone; on the other hand, conductivity in the air usually is set to be a small but nonzero value for MT modeling, however, the conductivity is set to be zero in the air for **T** − Ω method. Therefore, the two benefits enable this method need less memory and the curl-curl equations are less ill-conditioned in the air (Mitsuhata and Uchida, 2004).

2. MT modeling in 3D anisotropic media

The study domain is divided into two zones, namely the air zone and the earth zone as shown in Fig. 1. The conductivity $\tilde{\sigma}$ is zero in the air and S_c is the earth's surface. The magnetic permeability of vacuum is used for the whole domain.

2.1. Differential equations

Comparing with conduction currents, displacement currents are negligible for MT method whose frequency ranges from 10^{-3} Hz to 10^4 Hz. For the time-dependence of e^{-iwt}, therefore the diffusive Maxwell's equations are as follows,

$$\nabla \times \mathbf{E} = i\omega\mu_0\mathbf{H} \tag{1}$$

$$\nabla \times \mathbf{H} = \mathbf{J} = \tilde{\sigma}\mathbf{E} \tag{2}$$

$$\nabla \cdot \mathbf{H} = 0 \tag{3}$$

$$\nabla \cdot \tilde{\sigma}\mathbf{E} = 0 \tag{4}$$

where **E** is the electric field and **H** is the magnetic field; ω is the angular frequency; μ_0 is the magnetic permeability in the air; **J** is the electric current density; $\tilde{\sigma}$ is the conductivity tensor which can be defined by two methods, namely Yin (2000) and Pek and Santos (2002), respectively. The latter is adopted in this work where $\tilde{\sigma}$ is determined by six anisotropic parameters: three axial conductivities (σ_x,σ_y and σ_z) and three Euler's angles (α_S,α_D and α_L) (see Pek and Santos (2002) for detail).

The magnetic field **H** can be separated into the incident field $\mathbf{H}_0$ and the resultant magnetic field $\mathbf{H}_c$ (Mitsuhata and Uchida, 2004),

$$\mathbf{H} = \mathbf{H}_0 + \mathbf{H}_c \tag{5}$$

where $\mathbf{H}_c$ is produced by the electric current in the earth.

Therefore Eq. (2) can be separated into two equations,

$$\nabla \times \mathbf{H}_0 = 0 \tag{6}$$

$$\nabla \times \mathbf{H}_c = \mathbf{J} = \tilde{\sigma}\mathbf{E} \tag{7}$$

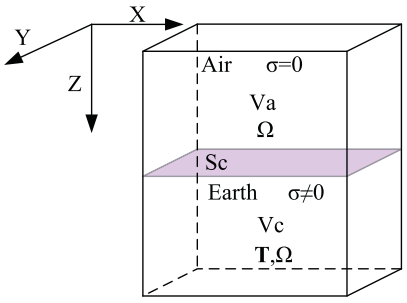

Fig. 1. Study domain: the zone Va is the air zone and Vc is the earth.

As $\nabla \cdot \mathbf{J} = 0$ is satisfied for MT method which has no electric current sources, therefore **J** can be represented by curling a vector,

$$\mathbf{J} = \nabla \times \mathbf{T} \tag{8}$$

where **T** is the electric vector potential.

Considering Eq. (7) and Eq. (8) together, then we can obtain Eq. (9) as follow,

$$\mathbf{H}_c = \mathbf{T} - \nabla\Omega \tag{9}$$

where Ω is the magnetic scalar potential.

After substituting Eq. (8) and Eq. (9) into Eq. (1), then the curl-curl equation can be obtained,

$$\nabla \times \left(\frac{1}{\tilde{\sigma}}\nabla \times \mathbf{T}\right) - i\omega\mu_0(\mathbf{T} - \nabla\Omega) = i\omega\mu_0\mathbf{H}_0 \ \text{ in } \ \mathrm{V_c} \tag{10}$$

As the conductivity in the air is zero, therefore Eq. (10) is only satisfied in the earth (Vc).

From Eq. (3) and Eq. (9), Eq. (11) can be obtained. As $\mathbf{T} = 0$ in the air zone, Eq. (11) is satisfied in the whole study domain.

$$\nabla \cdot (\mathbf{T} - \nabla\Omega) = 0 \quad \text{in} \quad \mathrm{V} \tag{11}$$

However, Eq. (9) and Eq. (11) are not independent of each other. For a flat earth surface, therefore Eq. (12) is adopted to obtain the unique solution combining with.

Eq. (9) (see Mitsuhata and Uchida (2004) for detail),

$$\nabla^2\Omega(\mathbf{r}) = T_z(\mathbf{r})\delta(\mathbf{r} \in \mathrm{S_c}) \quad \text{in} \quad \mathrm{V} \tag{12}$$

where δ is the Dirac delta function, and $\mathbf{T}_z$ denotes the z-component of **T**. Eq. (9) and Eq. (12) are used to obtain the unique solution.

2.2. Dirichlet boundary conditions

Ω and $\mathbf{T}_z$ both are produced by 2D or 3D conductivity anomalies (Mitushata and Uchida, 2004). Dirichlet conditions are adopted here. Assuming anomalies are far enough from the boundaries of *V*, therefore $\Omega = 0$ and $T_z = 0$ are satisfied at the boundaries. For T_x and T_y, we can obtain Eq. (13) and Eq. (14) from Eq. (5) and Eq. (9),

$$T_x = H_x - H_{0x} \tag{13}$$

$$T_y = H_y - H_{0y} \tag{14}$$

Two orthogonal sources are adopted here.

3. Finite element method

The Galerkin FE method is adopted to generate the variational equation (Xu, 1994), and nodal and edge elements are used to discrete the study domain.

3.1. Nodal and edge elements

As shown in Fig. 2, **T** is assigned at the twelve edges and Ω is assigned at the eight nodes. Then.

$$\mathbf{T}_e = \sum_{i=1}^{12} \mathbf{N}_e^i T_e^i \tag{15}$$

$$\Omega_e = \sum_{j=1}^{8} M_e^j \Omega_e^j \tag{16}$$

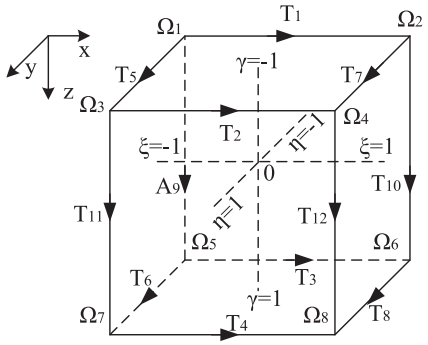

Fig. 2. Sampling points for **T** and Ω in the brick element and the local coordinate system (Mitsuhata and Uchida, 2004).

where **N** is the Whitney vector basis and *M* is the node basis (Jin, 2002).

3.2. Galerkin finite-element method

Eq. (10) and Eq. (12) are used to generate the stiffness matrix.

(1) Multiplying the both sides of Eq. (10) by $\delta\mathbf{T}$, then integrate it in V_c,

$$\int_{v_c}\left[\nabla\times\left(\frac{1}{\hat{\sigma}}\nabla\times\mathbf{T}\right)-i\omega\mu_0(\mathbf{T}-\nabla\Omega)-i\omega\mu_0\mathbf{H}_0\right]\cdot\delta\mathbf{T}dv=0 \tag{17}$$

Considering the vector identity and divergence theorem, then the first term of the left side of Eq. (15) is reverted to,

$$\int_{v_c}\nabla\times\left(\frac{1}{\hat{\sigma}}\nabla\times\mathbf{T}\right)\cdot\delta\mathbf{T}dv=\int_{v}\nabla\times\delta\mathbf{T}\cdot\frac{\nabla\times\mathbf{T}}{\hat{\sigma}}dv+\int_{s}\left(\frac{\nabla\times\mathbf{T}}{\hat{\sigma}}\right)\times\delta\mathbf{T}\cdot d\mathbf{s} \tag{18}$$

Substituting Eq. (18) into Eq. (17),

$$\int_{v_c}\left[\nabla\times\delta\mathbf{T}\cdot\frac{\nabla\times\mathbf{T}}{\hat{\sigma}}-i\omega\mu_0(\mathbf{T}-\nabla\Omega)\cdot\delta\mathbf{T}-i\omega\mu_0\mathbf{H}_0\cdot\delta\mathbf{T}\right]dv+\int_{s}\left(\frac{\nabla\times\mathbf{T}}{\hat{\sigma}}\right)\times\delta\mathbf{T}\cdot d\mathbf{s}=0 \tag{19}$$

Since counteraction, the second term regarding to the surface integral equals zero for inner boundaries. Besides, Dirichlet boundaries are adopted for outer boundaries, therefore.

$$\int_{v_c}\nabla\times\delta\mathbf{T}\cdot\frac{\nabla\times\mathbf{T}}{\hat{\sigma}}dv-i\omega\mu_0\int_{v_c}(\mathbf{T}-\nabla\Omega)\cdot\delta\mathbf{T}dv-i\omega\mu_0\int_{v_c}\mathbf{H}_0\cdot\delta\mathbf{T}dv=0 \tag{20}$$

(2) Multiplying the both sides of Eq. (12) by$\delta\Omega$, then integrate it in the whole study space,

$$-\int_{v}\nabla^2\Omega\delta\Omega dv+\int_{v}T_z(\mathbf{r})\delta(\mathbf{r}\in S_c)\delta\Omega dv=0 \tag{21}$$

Considering Green's theorem, then the first term of the left of Eq. (21) became,

$$\begin{aligned}-\int_{v}\nabla^2\Omega\delta\Omega dv&=-\int_{v}\nabla\cdot(\nabla\Omega\delta\Omega)dv+\int_{v}\nabla\Omega\cdot\nabla\delta\Omega dv\\&=\int_{v}\nabla\Omega\cdot\nabla\delta\Omega dv-\int_{s}\frac{\partial\Omega}{\partial n}\delta\Omega ds=\int_{v}\nabla\Omega\cdot\nabla\delta\Omega dv\end{aligned} \tag{22}$$

For the second term of the left of Eq. (21),

$$\int_{v}T_z(\mathbf{r})\delta(\mathbf{r}\in S_c)\delta\Omega dv=\int_{s_c}T_z\delta\Omega ds_c \tag{23}$$

Therefore, Eq. (21) became Eq. (24) which is identical to Eq. (23) in the paper of Bíró (1999),

$$\int_{v}\nabla\Omega\cdot\nabla\delta\Omega dv+\int_{s_c}T_z\delta\Omega ds_c=0 \tag{24}$$

For a given element, combining Eq. (20) and Eq. (24) we can get,

$$\begin{bmatrix}\mathbf{C}_e & \mathbf{D}_e\\ \mathbf{E}_e & \mathbf{F}_e+\mathbf{G}_e\end{bmatrix}\times\begin{bmatrix}\mathbf{\Omega}_e\\ \mathbf{T}_e\end{bmatrix}=\begin{bmatrix}\mathbf{0}\\ \mathbf{P}_e\end{bmatrix} \tag{25}$$

where $\mathbf{C}_e$, $\mathbf{D}_e$, $\mathbf{E}_e$, $\mathbf{F}_e$, $\mathbf{G}_e$, $\mathbf{\Omega}_e$, $\mathbf{T}_e$,and $\mathbf{P}_e$ are 8×8, 8×12, 12×8, 12×12, 12×12, 8×1, 12×1 and 12×1 matrixes, respectively. The details of Eq. (25) are given in Appendix A.

By applying the boundary conditions after expanding Eq. (25) to the whole space, finally Eq. (26) can be obtained as follow,

$$\mathbf{Ax}=\mathbf{b} \tag{26}$$

The linear system of equations is asymmetric, and**T** and Ω can be obtained after solving Eq. (26).

4. Apparent resistivities and phase

From Eq. (2) and Eq. (8), the electric field can be obtained as follows,

$$E_x=\frac{\left(\frac{\partial Ty}{\partial x}-\frac{\partial Tx}{\partial y}\right)(\sigma_{xy}\sigma_{yz}-\sigma_{xz}\sigma_{yy})+\left(\frac{\partial Tx}{\partial z}-\frac{\partial Tz}{\partial x}\right)(\sigma_{xz}\sigma_{zy}-\sigma_{xy}\sigma_{zz})+\left(\frac{\partial Tz}{\partial y}-\frac{\partial Ty}{\partial z}\right)(\sigma_{yy}\sigma_{zz}-\sigma_{yz}\sigma_{zy})}{\sigma_{xx}\sigma_{yy}\sigma_{zz}-\sigma_{xx}\sigma_{yz}\sigma_{zy}-\sigma_{xy}\sigma_{yx}\sigma_{zz}+\sigma_{xy}\sigma_{yz}\sigma_{zx}+\sigma_{xz}\sigma_{yx}\sigma_{zy}-\sigma_{xz}\sigma_{yy}\sigma_{zx}} \tag{27}$$

$$E_y=\frac{\left(\frac{\partial Ty}{\partial x}-\frac{\partial Tx}{\partial y}\right)(\sigma_{xz}\sigma_{yx}-\sigma_{xx}\sigma_{yz})+\left(\frac{\partial Tx}{\partial z}-\frac{\partial Tz}{\partial x}\right)(\sigma_{xx}\sigma_{zz}-\sigma_{xz}\sigma_{zx})+\left(\frac{\partial Tz}{\partial y}-\frac{\partial Ty}{\partial z}\right)(\sigma_{yz}\sigma_{zx}-\sigma_{yx}\sigma_{zz})}{\sigma_{xx}\sigma_{yy}\sigma_{zz}-\sigma_{xx}\sigma_{yz}\sigma_{zy}-\sigma_{xy}\sigma_{yx}\sigma_{zz}+\sigma_{xy}\sigma_{yz}\sigma_{zx}+\sigma_{xz}\sigma_{yx}\sigma_{zy}-\sigma_{xz}\sigma_{yy}\sigma_{zx}} \tag{28}$$

$$E_z=\frac{\left(\frac{\partial Ty}{\partial x}-\frac{\partial Tx}{\partial y}\right)(\sigma_{xx}\sigma_{yx}-\sigma_{xy}\sigma_{yx})+\left(\frac{\partial Tx}{\partial z}-\frac{\partial Tz}{\partial x}\right)(\sigma_{xy}\sigma_{zx}-\sigma_{xx}\sigma_{zy})+\left(\frac{\partial Tz}{\partial y}-\frac{\partial Ty}{\partial z}\right)(\sigma_{yx}\sigma_{zy}-\sigma_{yy}\sigma_{zx})}{\sigma_{xx}\sigma_{yy}\sigma_{zz}-\sigma_{xx}\sigma_{yz}\sigma_{zy}-\sigma_{xy}\sigma_{yx}\sigma_{zz}+\sigma_{xy}\sigma_{yz}\sigma_{zx}+\sigma_{xz}\sigma_{yx}\sigma_{zy}-\sigma_{xz}\sigma_{yy}\sigma_{zx}} \tag{29}$$

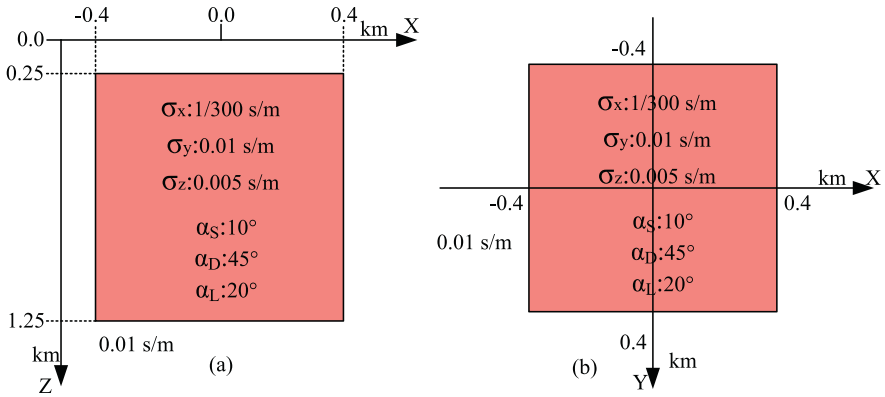

Fig. 3. 3D anisotropic model.

From Eq. (5) and Eq. (9), the magnetic fields can be obtained as follows,

$$H_x = H_{0x} + T_x - \frac{\partial \Omega}{\partial x} \tag{30}$$

$$H_y = H_{0y} + T_y - \frac{\partial \Omega}{\partial y} \tag{31}$$

$$H_z = H_{0z} + T_z - \frac{\partial \Omega}{\partial z} \tag{32}$$

Then we can obtain the impedance tensor, the apparent resistivities and phases (Li, 2002).

5. Numerical experiments

We first validated the accuracy and showed the merits of this algorithm for a generalized anisotropic 3D model. Then we studied two types of anisotropic models and analyzed the results in detail. The apparent resistivities showed in this paper are for the flat surface (S_c) along the air earth interface.

5.1. Test Model

In this section, the $\mathbf{T} - \Omega$ method's results are firstly compared with the results of the edge-based FE method (Xiao et al., 2018) for three different frequencies from high to low (100 Hz, 1 Hz and 0.001 Hz), respectively. Then, we showed the convergence of three frequencies. Finally, the divergence of the electric current is also shown to demonstrate that the $\mathbf{T} - \Omega$ method does maintain divergence free conditions. The results show that the $\mathbf{T} - \Omega$ method works well even for low frequencies and it does maintain divergence free conditions.

5.1.1. Validating the accuracy

An arbitrary anisotropic 3D model is designed to validate the accuracy of this method. As shown in Fig. 3, a 3D generalized anisotropic anomaly is embedded in an isotropic half-space of 0.01 S/m. The three axial conductivities of this anomaly are 1/300 s/m, 0.01 s/m and 0.005 s/m, respectively; the three Euler's angles (i.e., α_S, α_D, and α_L) are 10^o, 45^o, and 20^o, respectively; the dimensions of this anomaly are 800 m × 800 m × 1000 m; its top depth is 250 m. In particularly, the edge-based FE method's results here are obtained by the direct solver Mumps (Han et al., 2018); the $\mathbf{T} - \Omega$ algorithm's solutions are obtained by the quasi-minimum residual (QMR) method with the symmetric successive over-relaxation (SSOR) (Koldan et al., 2014; Liu et al., 2016). Two modes' (xy-mode and yx-mode) apparent resistivities on the ground surface (S_c) are compared here.

The three frequencies' results are showed in Fig. 4, Fig. 5 and Fig. 6, respectively. The first column corresponds to the apparent resistivities of $\mathbf{T} - \Omega$ algorithm; the second column corresponds to the apparent resistivites of the edge-based FE method (Xiao et al., 2018); the third column corresponds to the relative errors; the first row and the second row correspond to xy-mode and yx-mode, respectively. It showed a very close level for the two methods' results as the relative errors are

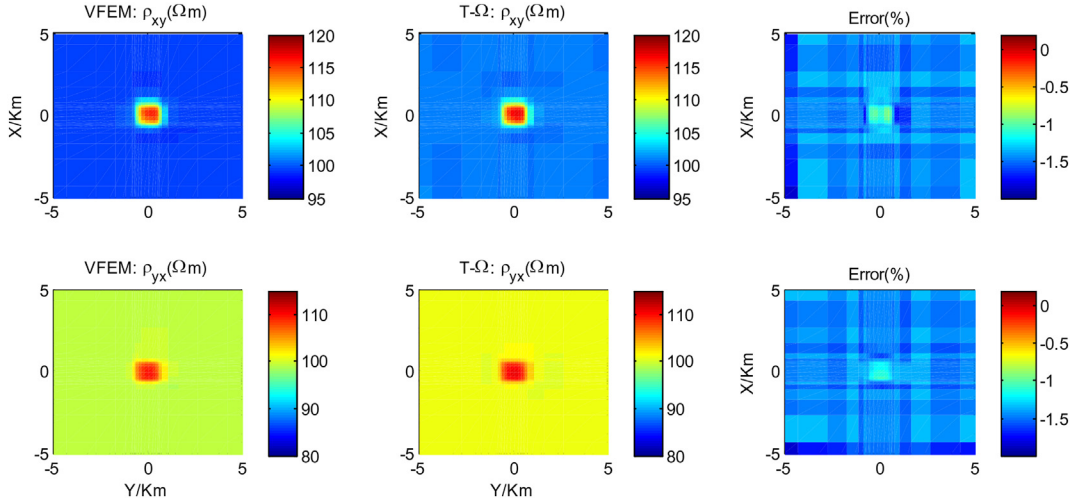

Fig. 4. The apparent reistivities of two methods at 100 Hz.

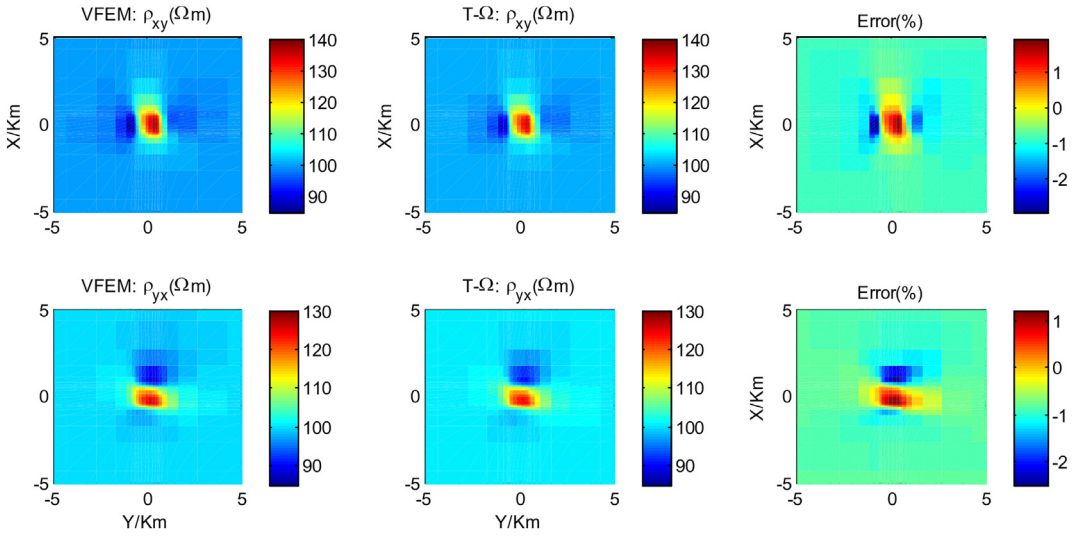

Fig. 5. The apparent reistivities of two methods at 1 Hz.

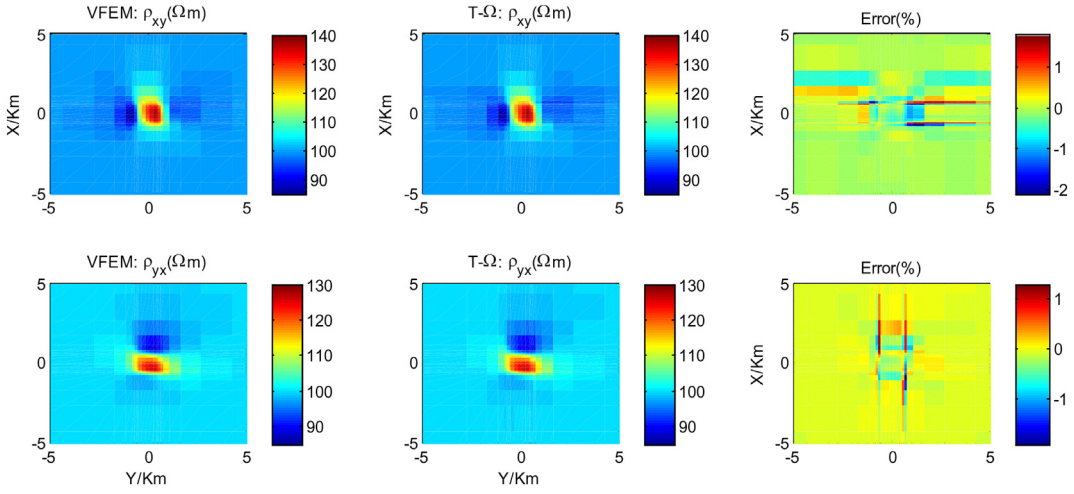

Fig. 6. The apparent reistivities of two methods at 0.001 Hz.

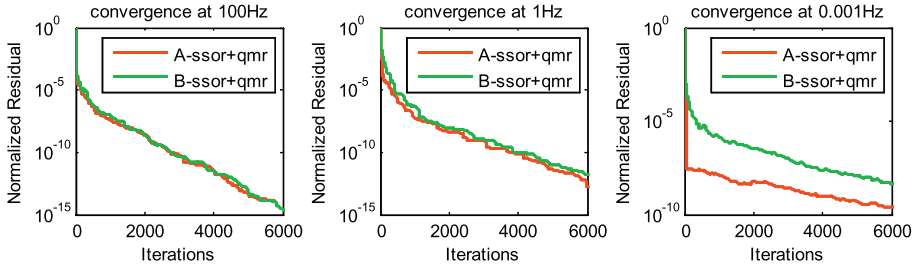

Fig. 7. Convergence plot of QMR solver with SSOR pre-conditioner for the data of different frequencies.

all less than 2.5% for three frequencies. It shows that even for a very low frequency 0.001 Hz the $\mathbf{T}-\Omega$ method still works well.

5.1.2. Convergence of the solution

Based on the Matlab platform, though the linear system of equations is asymmetric, the SSOR pre-conditioner still works stably here. As shown in Fig. 7, either xy-mode or yx-mode in each condition obtained a good convergence. Especially, for a very low frequency (0.001 Hz) the xy- and yx-mode also have a good convergence (less than 10^{-8}). The calculation was performed on a computer with Intel ® Core ™ i7-4790 3.60GHz processors. The number of cells is 25, 688, and the computational time for 3000 iterations is about 330 s.

5.1.3. Divergence of electric current

In order to demonstrate that the $\mathbf{T}-\Omega$ formulation does maintain divergence free conditions, the divergence of the electric current is

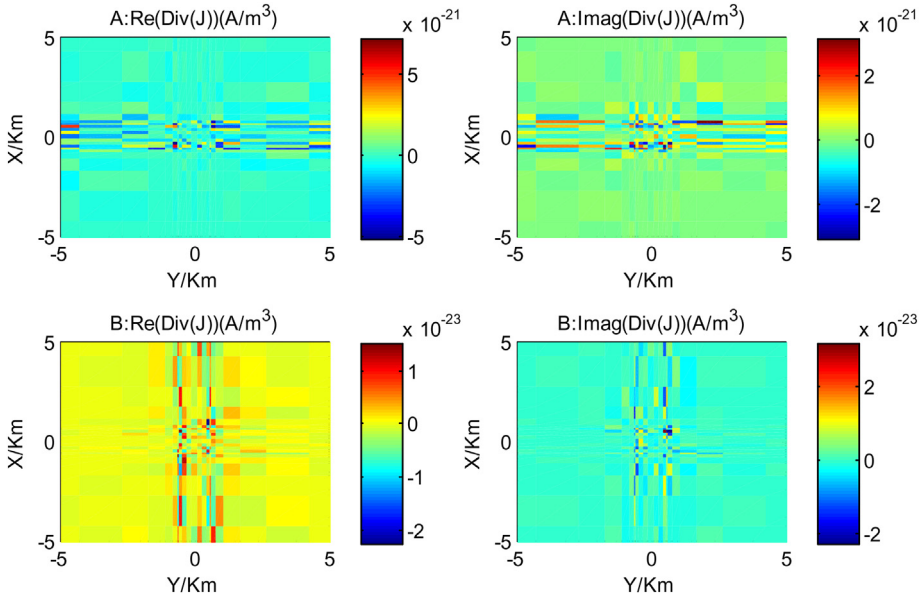

Fig. 8. The current's divergence of 100 iterations of 1 Hz at depth of 750 m: A and B denote the two modes of MT; Re and Imag represent the real part and the imaginary part of the divergence, respectively.

calculated (see Appendix B for details). We calculated the divergence for different iterations (e.g. 2, 5, 40, 100, 200, 400, 1000 and 2000 iterations), we found that the divergence values are really very small (less than10^{-20}). The data presented in Fig. 8 show the divergence of 100 iterations of 1 Hz at depth of 750 m. The divergence values are very small (less than 10^{-21}) and can be seen as zero. Therefore, the $\mathbf{T}-\Omega$ method does maintain divergence free conditions.

5.2. Anisotropic anomaly in isotropic layered media

In three-layered isotropic media, there is an anisotropic anomaly. As shown in Fig. 9: the conductivities of the three layers are 0.01 s/m, 0.02 s/m, and 0.005 s/m, respectively; the thicknesses of the first layer and the second layer are 550 m, 900 m, respectively; the dimensions of the 3D anomaly are 800 m, 800 m and 2000 m (x-, y-, and z-direction), respectively; the three axial conductivities of the anomaly are 0.01 s/m, 0.02 s/m, and 0.005 s/m, respectively. We studied these conditions that one of the three Euler's angles changes and the other two angles equal zero. Besides, we obtain another three isotropic models (Iso 1, Iso 2, and Iso 3) by setting the conductivity of the anisotropic anomaly to be 0.01 s/m, 0.02 s/m, and 0.005 s/m, respectively. The frequency used here is 1 Hz.

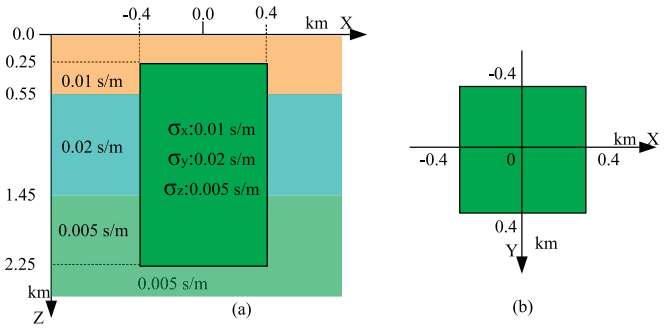

Fig. 9. An anisotropic anomaly in isotropic three-layered media: (a) section view; (b) plan view.

5.2.1. Angle α_S changes

The apparent resistivities of the anisotropic anomaly with a different angle α_S and the three isotropic models are shown in Fig. 10. Three symbols are used here: the white square represents the size and shape of that 3D anomaly; the angles between the red solid lines and the y-direction are 0°, 30°, 60°, and 90° from the first column to the fourth column, respectively; the angles between the blue solid lines and the x-direction are 0°, 30°, 60°, and 90° from the first column to the fourth column, respectively.

In Fig. 10, the first to the fourth column represents the apparent resistivities of xx-mode, xy-mode, yx-mode and yy-mode, respectively; the first to the fourth column represents the angle α_S equals 0°, 30°, 60°, and 90°, respectively; the fifth to the seventh column represents Iso 1 model, Iso 2 model, and Iso 3 model, respectively. As shown in this figure: (1) the distribution of the apparent resistivities can indicate the size and location of the 3D anisotropic anomaly; (2) as angle α_S changes, the red solid lines are able to indicate the distribution of the lower apparent resisvitities; (3) as angle α_S changes, the blue solid lines can indicate the distribution of the higher apparent resistivities; (4) when angle α_S equal 0°, the xy-mode and yy-mode apparent resistivitis are similar to the xy-mode and yy-mode apparent resistivities of Iso 1 model, respectively; (5) when angle α_S equal 0°, the yx-mode and xx-mode apparent resistivitis are similar to the yx-mode and xx-mode apparent resistivities of Iso 2 model, respectively; (6) when angle α_S equal 90°, the xy-mode and yy-mode apparent resistivities are similar to the xy-mode and yy-mode apparent resistivities of Iso 2 model, respectively; (7) when angle α_S equal 90°, the yx-mode and xx-mode apparent resistivities are similar to the yx-mode and xx-mode apparent resistivities of Iso 1 model, respectively.

In addition, we made some quantitative analyses for the 'similar' mentioned above. As shown in Fig. 11: (1) the first row corresponds to the comparison between ρ_{xy} when angle α_S is 0° and ρ_{xy} of Iso 1 model, and the relative error is less than 2%; (2) the second row corresponds to the comparison between ρ_{yx} when angle α_S is 0° and ρ_{yx} of Iso 2 model, and the relative error is less than 0.5%; (3) the third row corresponds to the comparison between $\rho_{xy}$when angle α_S is 90° and ρ_{xy} of Iso 2 model, and the relative error is less than 2%; (4) the fourth row corresponds to the comparison between ρ_{yx} when angle α_S is 90° and ρ_{yx} of Iso 1 model, and the relative error is less than 2%. The relative errors all are less than 2%.

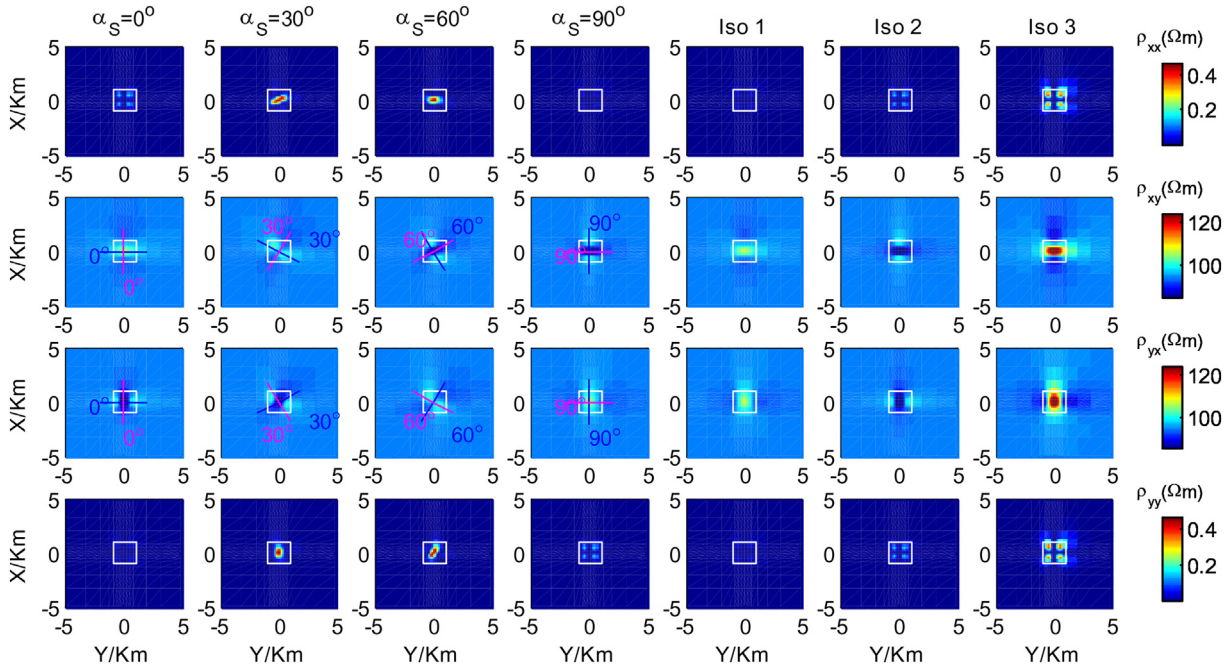

Fig. 10. The apparent resistivities of the anisotropic anomaly with a different angle α_S and the three isotropic models (Iso 1, Iso2, and Iso 3).

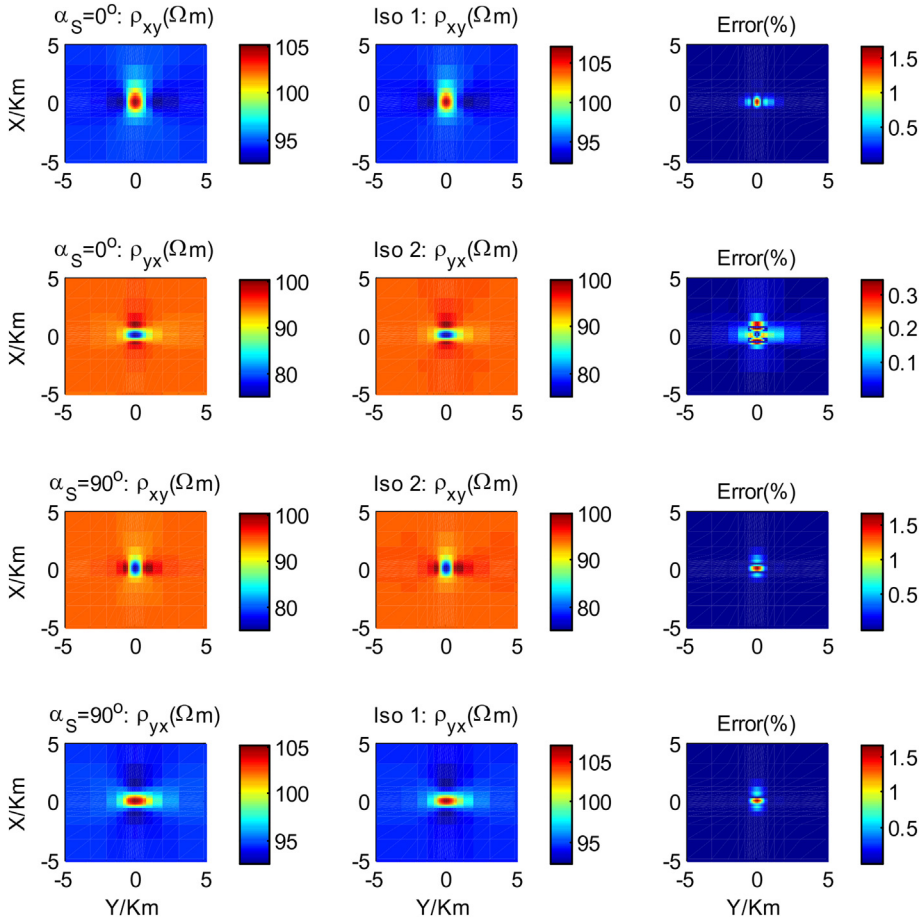

Fig. 11. The comparison of apparent resistivities (xy-mode and yx-mode) between axial anisotropy (α_S equals 0° or 90°) and isotropy (Iso 1 and Iso 2).

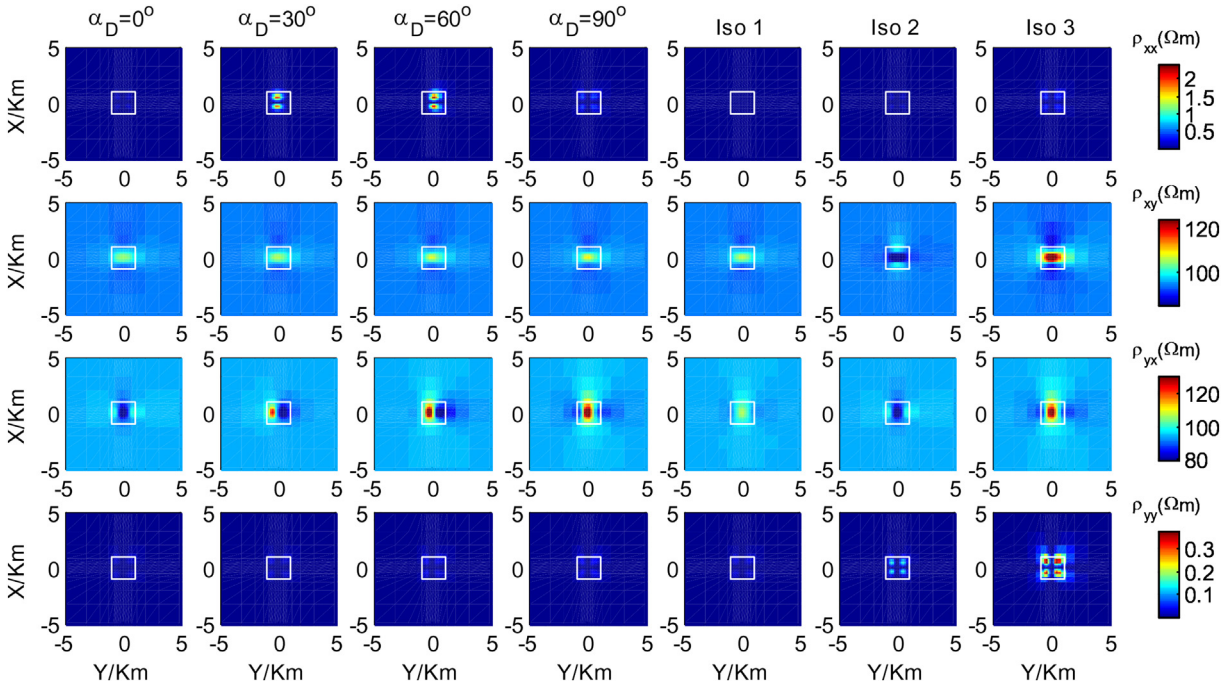

Fig. 12. The apparent resistivities of the anisotropic anomaly with a different angle α_D and the three isotropic models (Iso 1, Iso2, and Iso 3).

5.2.2. Angle α_D changes

The apparent resistivities of the anisotropic anomaly with a different angle α_S and the three isotropic models are shown in Fig. 12. The first to the fourth column represents the apparent resistivities of xx-mode, xy-mode, yx-mode and yy-mode, respectively; the first to the fourth column represents the angle α_D equals 0°, 30°, 60°, and 90°, respectively; the fifth to the seventh column represents Iso 1 model, Iso 2 model, and Iso 3 model, respectively.

As shown in Fig. 12: (1) the distributions of ρ_{xy} and ρ_{yx} are able to indicate the shape and location of the 3D anisotropic anomaly; (2) ρ_{xy} almost keeps unchanged as α_D changes, and is similar to ρ_{xy} of Iso 1 model; (3) ρ_{yy} keeps unchanged when α_D changes; (4) when angle α_D equals 90°, the xy-mode and yy-mode apparent resistivities are similar to the xy-mode and yy-mode apparent resistivities of Iso 1 model, respectively; (5) when angle α_D equals 90°, the yx-mode and xx-mode

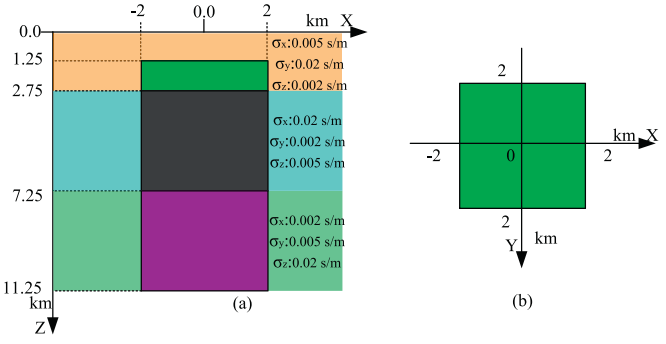

Fig. 14. Three isotropic anomalies in three-layered anisotropic media: (a) section view; (b) plan view.

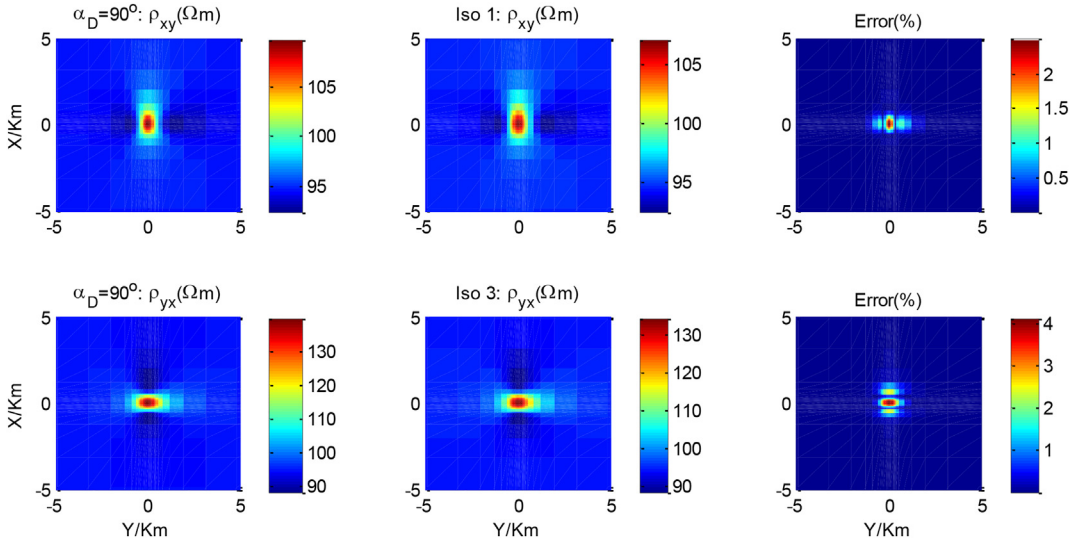

Fig. 13. The comparison of apparent resistivities (xy-mode and yx-mode) between axial anisotropy (α_D equals 0° or 90°) and isotropy (Iso 1 and Iso 3).

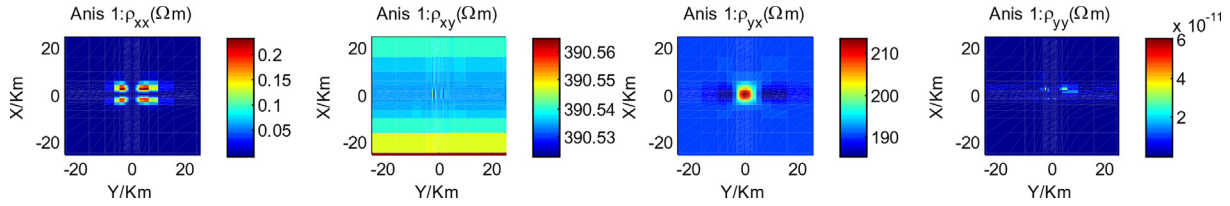

Fig. 15. The apparent resistivities of Anis 1 model.

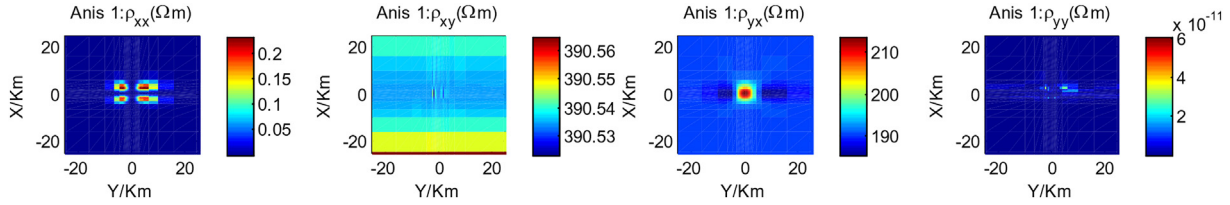

Fig. 16. The apparent resistivities of Anis 2 model.

apparent resistivities are similar to the yx-mode and xx-mode apparent resistivities of Iso 3 model, respectively.

In addition, we also made some quantitative analyses for the 'similar' mentioned above. As shown in Fig. 13: (1) the first row corresponds to the comparison between ρ_{xy} when angle α_D is 90° and ρ_{xy} of Iso 1 model, and the relative error is less than 2.5%; (2) the second row corresponds to the comparison between ρ_{yx} when angle α_D is 90° and ρ_{yx} of Iso 3 mdoel, and the relative error is less than 4%.

From the analyses in section 5.2.1 and section 5.2.2, we can conclude that the apparent resistivities ρ_{xy} and ρ_{yy} are mainly influenced by the conductivity in the x-direction, and the apparent resistivities ρ_{yx} and ρ_{xx} are mainly influenced by the conductivity in the y-direction.

5.3. Isotropic anomalies in anisotropic layered media

In three-layered axial anisotropic media, there are three isotropic anomalies. As shown in Fig. 14:

(1) the conductivities of the first layer are 0.005 s/m, 0.02 s/m, and 0.002 s/m, respectively; the conductivities of the second layer are 0.02 s/m, 0.002 s/m, and 0.005 s/m, respectively; the conductivities of the third layer are 0.002 s/m, 0/005 s/m, and 0.02 s/m, respectively; the thicknesses of the first layer and the second layer are 2750 m, and 4500 m, respectively.
(2) the dimensions of the first 3D anomaly (the green one) are 4000 m, 4000 m, and 1500 m in x-, y- and z-direction, respectively; the dimensions of the second 3D anomaly (the black one) are 4000 m, 4000 m, and 4500 m, respectively; the dimensions of the third 3D anomaly (the purple one) are 4000 m, 4000 m, and 4000 m, respectively; the top depths of the three 3D anomalies are 1250 m, 2750 m, and 7250 m, respectively. We emphasize that the first 3D anomaly, the second 3D anomaly, and the third 3D anomaly are embedded in the first layer, the second layer and the third layer, respectively.

Two models are obtained by setting the three isotropic anomalies to different conductivity values. The frequency used here is 0.001 Hz. In addition, the analytical solutions ρ_{xx}, ρ_{xy}, ρ_{yx}, and ρ_{yy} of the three-layered media without any anomalies are 0 $\Omega \cdot m$, 390.31 $\Omega \cdot m$, 190.39 $\Omega \cdot m$, and 0 $\Omega \cdot m$, respectively.

Anis 1 model: the conductivities of the three isotropic anomalies (green, black and purple) are set to be 0.005 s/m, 0.02 s/m, and 0.002 s/m, respectively. The apparent resistivities of this model are shown in Fig. 15: (1) ρ_{xy} keeps almost unchanged and is the same as ρ_{xy} (390.31 $\Omega \cdot m$) of the three-layered media; (2) ρ_{yy} can be considered as zero which is the same as ρ_{yy} (0 $\Omega \cdot m$) of the three-layered media. For theoretical analysis, this is because the conductivities of these three anomalies are the same as the principal conductivities σ_x of the first layer, the second layer and the third layer, respectively.

Anis 2 model: the conductivities of these three isotropic anomalies are set to be 0.02 s/m, 0.002 s/m, and 0.005 s/m, respectively. The apparent resistivities of this model are shown in Fig. 16: (1) ρ_{yx} remains almost unchanged and is the same as ρ_{yx} (390.31 $\Omega \cdot m$) of the three-layered media; (2) ρ_{xx} can be considered as zero which is the same as ρ_{xx} (190.39 $\Omega \cdot m$) of the three-layered media. For theoretical analysis, this is because the conductivities of these three anomalies are the same as the principal conductivities σ_y of the first layer, the second layer and the third layer, respectively.

From the analyses above, for a 3D isotropic anomalies embedded in an axial anisotropic layered-media we can conclude that: (1) if the anomaly's conductivity is the same as the principal conductivity σ_x of the layered-media, then this anomaly almost have no influence on the apparent resistivities ρ_{xy} and ρ_{yy}; (2) if the anomaly's conductivity is the same as the principal conductivity σ_y of the layered-media, then this anomaly almost have no influence on the apparent resistivities ρ_{yx} and ρ_{xx}.

6. Conclusions

For 3D MT modeling in arbitrary anisotropic media, we successfully developed an algorithm using the T-Ω FE method. Then its accuracy was validated by comparing its solutions with the results of the edge-based FE method for a 3D generalized anisotropic model. Later, two types of models are studied and the results are analyzed in detail. Finally, considering the analyses together we can conclude two main conclusions: (1) if the anomaly's one principal conductivity (σ_x, or σ_y, or σ_z) is in the x-direction, then its other anisotropic parameters almost have no influence on the apparent resistivities of ρ_{xy} and ρ_{xx}; (2) if the anomaly's one principal conductivity is in the y-direction, then its other anisotropic parameters almost have no influence on the apparent resistivities of ρ_{yx} and ρ_{xx}.

Acknowledgements

Thanks to Dr. Josef Pek for his 1D MT anisotropic modeling code. Also thanks to Dr. Kong Wenxin for his positive discussion. This study is co-funded by the National Key Research and Development Project of China (2016YFC0600301) and the National Natural Science Foundation of China (No. 41425017).

Appendix A. Appendix

In this section, the details and specific values of these matrixes in Eq. (25) are given, i.e.$\mathbf{C}_e$, $\mathbf{D}_e$, $\mathbf{E}_e$, $\mathbf{F}_e$, $\mathbf{G}_e$, $\mathbf{\Omega}_e$, $\mathbf{T}_e$,and $\mathbf{P}_e$. Especially, $\mathbf{C}_e$, $\mathbf{D}_e$, $\mathbf{E}_e$, $\mathbf{F}_e$, $\mathbf{G}_e$, $\mathbf{\Omega}_e$, $\mathbf{T}_e$,and $\mathbf{P}_e$ are 8×8, 8×12, 12×8, 12×12, 12×12, 8×1, 12×1 and 12×1 matrixes, respectively; a, b and c are the length, width and height of the rectangular cell, respectively

(1) For $\frac{1}{\hat{\sigma}}$, it can be writen as,

$$\frac{1}{\hat{\sigma}} = \hat{\sigma}^{-1} = \begin{pmatrix} \sigma_{inv}^{xx} & \sigma_{inv}^{xy} & \sigma_{inv}^{xz} \\ \sigma_{inv}^{yx} & \sigma_{inv}^{yy} & \sigma_{inv}^{yz} \\ \sigma_{inv}^{zx} & \sigma_{inv}^{zy} & \sigma_{inv}^{zz} \end{pmatrix} \tag{A1}$$

(2) For $\mathbf{F}_e$,

$$\begin{aligned} \mathbf{F}_e &= \int_{V_c^e} \left(\nabla \times \mathbf{N}_e^i\right) \cdot \left(\frac{\nabla \times \mathbf{N}_e^j}{\hat{\sigma}}\right) dv \\ &= \int_{v_c} \sum_{i=1}^{4} \sum_{j=1}^{4} \left\{ \begin{pmatrix} \mathbf{0} & \frac{\partial N_e^i}{\partial z} & -\frac{\partial N_e^i}{\partial y} \\ -\frac{\partial N_e^{4+i}}{\partial z} & \mathbf{0} & \frac{\partial N_e^{4+i}}{\partial x} \\ \frac{\partial N_e^{8+i}}{\partial y} & -\frac{\partial N_e^{8+i}}{\partial x} & \mathbf{0} \end{pmatrix} \begin{pmatrix} \sigma_{inv}^{xx} & \sigma_{inv}^{xy} & \sigma_{inv}^{xz} \\ \sigma_{inv}^{yx} & \sigma_{inv}^{yy} & \sigma_{inv}^{yz} \\ \sigma_{inv}^{zx} & \sigma_{inv}^{zy} & \sigma_{inv}^{zz} \end{pmatrix} \begin{pmatrix} \mathbf{0} & -\frac{\partial N_e^{4+j}}{\partial z} & \frac{\partial N_e^{8+j}}{\partial y} \\ \frac{\partial N_e^j}{\partial z} & \mathbf{0} & -\frac{\partial N_e^{8+j}}{\partial x} \\ -\frac{\partial N_e^j}{\partial y} & \frac{\partial N_e^{4+j}}{\partial x} & \mathbf{0} \end{pmatrix} \right\} dv_c \\ &= \begin{pmatrix} \mathbf{F}_e^{xx} & \mathbf{F}_e^{xy} & \mathbf{F}_e^{xz} \\ \mathbf{F}_e^{yx} & \mathbf{F}_e^{yy} & \mathbf{F}_e^{yz} \\ \mathbf{F}_e^{zx} & \mathbf{F}_e^{zy} & \mathbf{F}_e^{zz} \end{pmatrix} \end{aligned} \tag{A2}$$

where

$$F_e^{xx} = \sigma_{inv}^{yy} \frac{ab}{6c} \begin{pmatrix} 2 & 1 & -2 & -1 \\ 1 & 2 & -1 & -2 \\ -2 & -1 & 2 & 1 \\ -1 & -2 & 1 & 2 \end{pmatrix} + \sigma_{inv}^{zy} \frac{a}{4} \begin{pmatrix} -1 & -1 & 1 & 1 \\ 1 & 1 & -1 & -1 \\ -1 & -1 & 1 & 1 \\ 1 & 1 & -1 & -1 \end{pmatrix} + \sigma_{inv}^{yz} \frac{a}{4} \begin{pmatrix} -1 & 1 & -1 & 1 \\ -1 & 1 & -1 & 1 \\ 1 & -1 & 1 & -1 \\ 1 & -1 & 1 & -1 \end{pmatrix} + \sigma_{inv}^{zz} \frac{ac}{6b} \begin{pmatrix} 2 & -2 & 1 & -1 \\ -2 & 2 & -1 & 1 \\ 1 & -1 & 2 & -2 \\ -1 & 1 & -2 & 2 \end{pmatrix} \tag{A3}$$

$$F_e^{yx} = \sigma_{inv}^{xy} \frac{ab}{4c} \begin{pmatrix} -1 & -1 & 1 & 1 \\ 1 & 1 & -1 & -1 \\ -1 & -1 & 1 & 1 \\ 1 & 1 & -1 & -1 \end{pmatrix} + \sigma_{inv}^{zy} \frac{b}{4} \begin{pmatrix} 1 & 1 & -1 & -1 \\ 1 & 1 & -1 & -1 \\ -1 & -1 & 1 & 1 \\ -1 & -1 & 1 & 1 \end{pmatrix} + \sigma_{inv}^{xz} \frac{a}{4} \begin{pmatrix} 1 & -1 & 1 & -1 \\ -1 & 1 & -1 & 1 \\ 1 & -1 & 1 & -1 \\ -1 & 1 & -1 & 1 \end{pmatrix} + \sigma_{inv}^{zz} \frac{c}{6} \begin{pmatrix} -2 & 2 & -1 & 1 \\ -1 & 1 & -2 & 2 \\ 2 & -2 & 1 & -1 \\ 1 & -1 & 2 & -2 \end{pmatrix} \tag{A4}$$

$$F_e^{zx} = \sigma_{inv}^{xy} \frac{a}{4} \begin{pmatrix} 1 & 1 & -1 & -1 \\ 1 & 1 & -1 & -1 \\ -1 & -1 & 1 & 1 \\ -1 & -1 & 1 & 1 \end{pmatrix} + \sigma_{inv}^{yy} \frac{b}{6} \begin{pmatrix} -2 & -1 & 2 & 1 \\ 2 & 1 & -2 & -1 \\ -1 & -2 & 1 & 2 \\ 1 & 2 & -1 & -2 \end{pmatrix} + \sigma_{inv}^{xz} \frac{ac}{4b} \begin{pmatrix} -1 & 1 & -1 & 1 \\ -1 & 1 & -1 & 1 \\ 1 & -1 & 1 & -1 \\ 1 & -1 & 1 & -1 \end{pmatrix} + \sigma_{inv}^{yz} \frac{c}{4} \begin{pmatrix} 1 & -1 & 1 & -1 \\ -1 & 1 & -1 & 1 \\ 1 & -1 & 1 & -1 \\ -1 & 1 & -1 & 1 \end{pmatrix} \tag{A5}$$

$$F_e^{xy} = \sigma_{inv}^{yx} \frac{ab}{4c} \begin{pmatrix} -1 & 1 & -1 & 1 \\ -1 & 1 & -1 & 1 \\ 1 & -1 & 1 & -1 \\ 1 & -1 & 1 & -1 \end{pmatrix} + \sigma_{inv}^{zx} \frac{a}{4} \begin{pmatrix} 1 & -1 & 1 & -1 \\ -1 & 1 & -1 & 1 \\ 1 & -1 & 1 & -1 \\ -1 & 1 & -1 & 1 \end{pmatrix} + \sigma_{inv}^{yz} \frac{b}{4} \begin{pmatrix} 1 & 1 & -1 & -1 \\ 1 & 1 & -1 & -1 \\ -1 & -1 & 1 & 1 \\ -1 & -1 & 1 & 1 \end{pmatrix} + \sigma_{inv}^{zz} \frac{c}{6} \begin{pmatrix} -2 & -1 & 2 & 1 \\ 2 & 1 & -2 & -1 \\ -1 & -2 & 1 & 2 \\ 1 & 2 & -1 & -2 \end{pmatrix} \tag{A6}$$

$$F_e^{yy} = \sigma_{inv}^{xx} \frac{ab}{6c} \begin{pmatrix} 2 & -2 & 1 & -1 \\ -2 & 2 & -1 & 1 \\ 1 & -1 & 2 & -2 \\ -1 & 1 & -2 & 2 \end{pmatrix} + \sigma_{inv}^{zx} \frac{b}{4} \begin{pmatrix} -1 & 1 & -1 & 1 \\ -1 & 1 & -1 & 1 \\ 1 & -1 & 1 & -1 \\ 1 & -1 & 1 & -1 \end{pmatrix} + \sigma_{inv}^{xz} \frac{b}{4} \begin{pmatrix} -1 & -1 & 1 & 1 \\ 1 & 1 & -1 & -1 \\ -1 & -1 & 1 & 1 \\ 1 & 1 & -1 & -1 \end{pmatrix} + \sigma_{inv}^{zz} \frac{bc}{6a} \begin{pmatrix} 2 & 1 & -2 & -1 \\ 1 & 2 & -1 & -2 \\ -2 & -1 & 2 & 1 \\ -1 & -2 & 1 & 2 \end{pmatrix} \tag{A7}$$

$$F_e^{zy} = \sigma_{inv}^{xx} \frac{a}{6} \begin{pmatrix} -2 & 2 & -1 & 1 \\ -1 & 1 & -2 & 2 \\ 2 & -2 & 1 & -1 \\ 1 & -1 & 2 & -2 \end{pmatrix} + \sigma_{inv}^{yx} \frac{b}{4} \begin{pmatrix} 1 & -1 & 1 & -1 \\ -1 & 1 & -1 & 1 \\ 1 & -1 & 1 & -1 \\ -1 & 1 & -1 & 1 \end{pmatrix} + \sigma_{inv}^{xz} \frac{c}{4} \begin{pmatrix} 1 & 1 & -1 & -1 \\ 1 & 1 & -1 & -1 \\ -1 & -1 & 1 & 1 \\ -1 & -1 & 1 & 1 \end{pmatrix} + \sigma_{inv}^{yz} \frac{bc}{4a} \begin{pmatrix} -1 & -1 & 1 & 1 \\ 1 & 1 & -1 & -1 \\ -1 & -1 & 1 & 1 \\ 1 & 1 & -1 & -1 \end{pmatrix} \tag{A8}$$

$$F_e^{xz} = \sigma_{inv}^{yx} \frac{a}{4} \begin{pmatrix} 1 & 1 & -1 & -1 \\ 1 & 1 & -1 & -1 \\ -1 & -1 & 1 & 1 \\ -1 & -1 & 1 & 1 \end{pmatrix} + \sigma_{inv}^{zx} \frac{ac}{4b} \begin{pmatrix} -1 & -1 & 1 & 1 \\ 1 & 1 & -1 & -1 \\ -1 & -1 & 1 & 1 \\ 1 & 1 & -1 & -1 \end{pmatrix} + \sigma_{inv}^{yy} \frac{b}{6} \begin{pmatrix} -2 & 2 & -1 & 1 \\ -1 & 1 & -2 & 2 \\ 2 & -2 & 1 & -1 \\ 1 & -1 & 2 & -2 \end{pmatrix} + \sigma_{inv}^{zy} \frac{c}{4} \begin{pmatrix} 1 & -1 & 1 & -1 \\ -1 & 1 & -1 & 1 \\ 1 & -1 & 1 & -1 \\ -1 & 1 & -1 & 1 \end{pmatrix} \tag{A9}$$

$$F_e^{yz} = \sigma_{inv}^{xx} \frac{a}{6} \begin{pmatrix} -2 & -1 & 2 & 1 \\ 2 & 1 & -2 & -1 \\ -1 & -2 & 1 & 2 \\ 1 & 2 & -1 & -2 \end{pmatrix} + \sigma_{inv}^{zx} \frac{c}{4} \begin{pmatrix} 1 & 1 & -1 & -1 \\ 1 & 1 & -1 & -1 \\ -1 & -1 & 1 & 1 \\ -1 & -1 & 1 & 1 \end{pmatrix} + \sigma_{inv}^{xy} \frac{b}{4} \begin{pmatrix} 1 & -1 & 1 & -1 \\ -1 & 1 & -1 & 1 \\ 1 & -1 & 1 & -1 \\ -1 & 1 & -1 & 1 \end{pmatrix} + \sigma_{inv}^{zy} \frac{bc}{4a} \begin{pmatrix} -1 & 1 & -1 & 1 \\ -1 & 1 & -1 & 1 \\ 1 & -1 & 1 & -1 \\ 1 & -1 & 1 & -1 \end{pmatrix} \tag{A10}$$

$$F_e^{zz} = \sigma_{inv}^{xx} \frac{ac}{6b} \begin{pmatrix} 2 & 1 & -2 & -1 \\ 1 & 2 & -1 & -2 \\ -2 & -1 & 2 & 1 \\ -1 & -2 & 1 & 2 \end{pmatrix} + \sigma_{inv}^{yx} \frac{c}{4} \begin{pmatrix} -1 & -1 & 1 & 1 \\ 1 & 1 & -1 & -1 \\ -1 & -1 & 1 & 1 \\ 1 & 1 & -1 & -1 \end{pmatrix} + \sigma_{inv}^{xy} \frac{c}{4} \begin{pmatrix} -1 & 1 & -1 & 1 \\ -1 & 1 & -1 & 1 \\ 1 & -1 & 1 & -1 \\ 1 & -1 & 1 & -1 \end{pmatrix} + \sigma_{inv}^{yy} \frac{bc}{6a} \begin{pmatrix} 2 & -2 & 1 & -1 \\ -2 & 2 & -1 & 1 \\ 1 & -1 & 2 & -2 \\ -1 & 1 & -2 & 2 \end{pmatrix} \tag{A11}$$

(3) For $\mathbf{G}_e$,

$$\begin{aligned} \mathbf{G}_e &= -i\omega\mu_0 \int_{V_c^e} \mathbf{N}_e^i \cdot \mathbf{N}_e^j dv \\ &= -\int_{v_c} i\omega\mu_0 \sum_{i=1}^{4} \sum_{j=1}^{4} \begin{bmatrix} N_e^i N_e^j & 0 & 0 \\ 0 & N_e^{4+i} N_e^{4+j} & 0 \\ 0 & 0 & N_e^{8+i} N_e^{8+j} \end{bmatrix} dv_c \\ &= -i\omega\mu_0 \begin{bmatrix} \mathbf{G}_e^{xx} & \mathbf{G}_e^{xy} & \mathbf{G}_e^{xz} \\ \mathbf{G}_e^{yx} & \mathbf{G}_e^{yy} & \mathbf{G}_e^{yz} \\ \mathbf{G}_e^{zx} & \mathbf{G}_e^{zy} & \mathbf{G}_e^{zz} \end{bmatrix} \end{aligned} \tag{A12}$$

where

$$\begin{aligned} \mathbf{G}_e^{xx} &= \mathbf{G}_e^{yy} = \mathbf{G}_e^{zz} \\ &= \frac{abc}{36} \begin{bmatrix} 4 & 2 & 2 & 1 \\ 2 & 4 & 1 & 2 \\ 2 & 1 & 4 & 2 \\ 1 & 2 & 2 & 4 \end{bmatrix} \end{aligned} \tag{A13}$$

$$\mathbf{G}_e^{xy}=\mathbf{G}_e^{xz}=\mathbf{G}_e^{yx}=\mathbf{G}_e^{yz}=\mathbf{G}_e^{zx}=\mathbf{G}_e^{zy}=\begin{bmatrix}0&0&0&0\\0&0&0&0\\0&0&0&0\\0&0&0&0\end{bmatrix} \tag{A14}$$

(4) For $\mathbf{E}_e$,

$$\mathbf{E}_e=i\omega\mu_0\int_{V_c^e}\mathbf{N}_e^i\cdot\nabla M_e^j dv=i\omega\mu_0\int_{v_c}\sum_{i=1}^{4}\sum_{j}^{8}\begin{pmatrix}N_e^i\dfrac{\partial M_e^j}{\partial x}\\N_e^{4+i}\dfrac{\partial M_e^{4+j}}{\partial y}\\N_e^{8+i}\dfrac{\partial M_e^{8+j}}{\partial z}\end{pmatrix}dv_c$$

$$=i\omega\mu_0\begin{pmatrix}\mathbf{E}_e^x\\\mathbf{E}_e^y\\\mathbf{E}_e^z\end{pmatrix} \tag{A15}$$

where

$$\mathbf{E}_e^x=\frac{bc}{36}\begin{pmatrix}-4&4&2&-2&-2&2&1&-1\\-2&2&4&-4&-1&1&2&-2\\-2&2&1&-1&-4&4&2&-2\\-1&1&2&-2&-2&2&4&-4\end{pmatrix} \tag{A16}$$

$$\mathbf{E}_e^y=\frac{ac}{36}\begin{pmatrix}-4&-2&2&4&-2&-1&1&2\\-2&-1&1&2&-4&-2&2&4\\-2&-4&4&2&-1&-2&2&1\\-1&-2&2&1&-2&-4&4&2\end{pmatrix} \tag{A17}$$

$$\mathbf{E}_e^z=\frac{ab}{36}\begin{pmatrix}-4&-2&-1&-2&4&2&1&2\\-2&-4&-2&-1&2&4&2&1\\-2&-1&-2&-4&2&1&2&4\\-1&-2&-4&-2&1&2&4&2\end{pmatrix} \tag{A18}$$

(5) For $\mathbf{P}_e$,

$$\mathbf{P}_e=i\omega\mu_0\int_{V_c^e}\mathbf{N}_e^i\cdot\mathbf{H}_0 dv=i\omega\mu_0\int_{v_c}\sum_{i=1}^{4}\sum_{j=1}^{4}\begin{bmatrix}N_{xi}N_{xj}&\mathbf{0}&\mathbf{0}\\\mathbf{0}&N_{yi}N_{yj}&\mathbf{0}\\\mathbf{0}&\mathbf{0}&N_{zi}N_{zj}\end{bmatrix}\begin{bmatrix}H_{0xi}\\H_{0yi}\\H_{0zi}\end{bmatrix}dv_c$$

$$=i\omega\mu_0\frac{abc}{36}\begin{bmatrix}4&2&2&1&0&0&0&0&0&0&0&0\\2&4&1&2&0&0&0&0&0&0&0&0\\2&1&4&2&0&0&0&0&0&0&0&0\\1&2&2&4&0&0&0&0&0&0&0&0\\0&0&0&0&4&2&2&1&0&0&0&0\\0&0&0&0&2&4&1&2&0&0&0&0\\0&0&0&0&2&1&4&2&0&0&0&0\\0&0&0&0&1&2&2&4&0&0&0&0\\0&0&0&0&0&0&0&0&4&2&2&1\\0&0&0&0&0&0&0&0&2&4&1&2\\0&0&0&0&0&0&0&0&2&1&4&2\\0&0&0&0&0&0&0&0&1&2&2&4\end{bmatrix}\begin{bmatrix}H_{0e}^1\\H_{0e}^2\\H_{0e}^3\\H_{0e}^4\\H_{0e}^5\\H_{0e}^6\\H_{0e}^7\\H_{0e}^8\\H_{0e}^9\\H_{0e}^{10}\\H_{0e}^{11}\\H_{0e}^{12}\end{bmatrix} \tag{A19}$$

(6) For $\mathbf{C}_e$,

$$\mathbf{C}_e=\int_{V^e}\nabla M_e^i\cdot\nabla M_e^j dv$$

$$=\int_{v^e}\sum_{i=1}^{8}\sum_{j=1}^{8}\left(\frac{\partial M_e^i}{\partial x}\frac{\partial M_e^j}{\partial x}+\frac{\partial M_e^i}{\partial y}\frac{\partial M_e^j}{\partial y}+\frac{\partial M_e^i}{\partial z}\frac{\partial M_e^j}{\partial z}\right)dv^e$$

$$=\frac{bc}{36a}\begin{pmatrix}4&-4&-2&2&2&-2&-1&1\\-4&4&2&-2&-2&2&1&-1\\-2&2&4&-4&-1&1&2&-2\\2&-2&-4&4&1&-1&-2&2\\2&-2&-1&1&4&-4&-2&2\\-2&2&1&-1&-4&4&2&-2\\-1&1&2&-2&-2&2&4&-4\\1&-1&-2&2&2&-2&-4&4\end{pmatrix}$$

$$+\frac{ac}{36b}\begin{pmatrix}4&2&-2&-4&2&1&-1&-2\\2&4&-4&-2&1&2&-2&-1\\-2&-4&4&2&-1&-2&2&1\\-4&-2&2&4&-2&-1&1&2\\2&1&-1&-2&4&2&-2&-4\\1&2&-2&-1&2&4&-4&-2\\-1&-2&2&1&-2&-4&4&2\\-2&-1&1&2&-4&-2&2&4\end{pmatrix}$$

$$+\frac{ab}{36c}\begin{pmatrix}4&2&1&2&-4&-2&-1&-2\\2&4&2&1&-2&-4&-2&-1\\1&2&4&2&-1&-2&-4&-2\\2&1&2&4&-2&-1&-2&-4\\-4&-2&-1&-2&4&2&1&2\\-2&-4&-2&-1&2&4&2&1\\-1&-2&-4&-2&1&2&4&2\\-2&-1&-2&-4&2&1&2&4\end{pmatrix} \tag{A20}$$

(7) For $\mathbf{D}_e$,

$$\mathbf{D}_e=\begin{cases}\int_{s_c}M_e^i\mid\mathbf{N}_e^j\mid ds & (\mathrm{i}=1,\cdots,4\ \text{and}\ \mathrm{j}=9,\cdots,12)\\ 0 & (\text{otherwise})\end{cases}$$

$$=\begin{cases}\int_{s_c}\sum_{i=1}^{4}\sum_{j=9}^{12}M_e^i\mid\mathbf{N}_e^j\mid ds_c & (\mathrm{i}=1,\cdots,4\ \text{and}\ \mathrm{j}=9,\cdots,12)\\ 0 & (\text{otherwise})\end{cases}$$

$$=\frac{ab}{36}\begin{pmatrix}0&0&0&0&0&0&0&0&4&2&2&1\\0&0&0&0&0&0&0&0&2&4&1&2\\0&0&0&0&0&0&0&0&1&2&2&4\\0&0&0&0&0&0&0&0&2&1&4&2\\0&0&0&0&0&0&0&0&0&0&0&0\\0&0&0&0&0&0&0&0&0&0&0&0\\0&0&0&0&0&0&0&0&0&0&0&0\\0&0&0&0&0&0&0&0&0&0&0&0\end{pmatrix} \tag{A21}$$

Appendix B. Appendix

In this section, we show how to calculate the electric current's divergence. As shown in Fig. B1, **T** is assigned at twelve edges

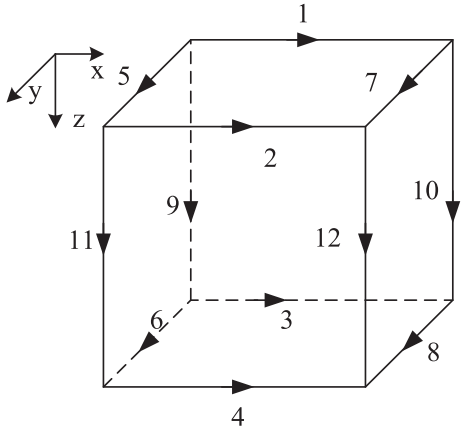

Fig. B1. Electric vector potential **T** at twelve edges of a brick element: 1: $T_x(i,j,k)$; 2: $T_x(i,j+1,k)$; 3: $T_x(i,j,k+1)$; 4: $T_x(i,j+1,k+1)$; 5: $T_y(i,j,k)$; 6: $T_y(i+1,j,k)$; 7: $T_y(i,j,k+1)$; 8: $T_y(i+1,j,k+1)$; 9: $T_z(i,j,k)$; 10: $T_z(i+1,j,k)$; 11: $T_z(i,j+1,k)$; 12: $T_z(i+1,j+1,k)$.

From Eq. 8, Eq. B1 can be obtained,

$$\nabla \cdot \mathbf{J} = \nabla \cdot \nabla \times \mathbf{T} = \frac{\partial}{\partial x}\left(\frac{\partial T_z}{\partial y} - \frac{\partial T_y}{\partial z}\right) + \frac{\partial}{\partial y}\left(\frac{\partial T_x}{\partial z} - \frac{\partial T_z}{\partial x}\right) + \frac{\partial}{\partial z}\left(\frac{\partial T_y}{\partial x} - \frac{\partial T_x}{\partial y}\right) \tag{B1}$$

Therefore, the divergence of the electric current in a cell can be calculated by Eq. (B2),.

$$\begin{aligned}\nabla \cdot \mathbf{J}_e = {} & (((T_z(i+1,j+1,k) - T_z(i+1,j,k))/b - (T_y(i+1,j,k+1) - T_y(i+1,j,k))/c) - \\ & ((T_z(i,j+1,k) - T_z(i,j,k))/b - (T_y(i,j,k+1) - T_y(i,j,k))/c))/a + \\ & (((T_x(i,j+1,k+1) - T_x(i,j+1,k))/c - (T_z(i+1,j+1,k) - T_z(i,j+1,k))/a) - \\ & ((T_x(i,j,k+1) - T_x(i,j,k))/c - (T_z(i+1,j,k) - T_z(i,j,k))/a))/b + \\ & (((T_y(i+1,j,k+1) - T_y(i,j,k+1))/a - (T_x(i,j+1,k+1) - T_x(i,j,k+1))/b) - \\ & ((T_y(i+1,j,k) - T_y(i,j,k))/a - (T_x(i,j+1,k) - T_x(i,j,k))/b))/c\end{aligned} \tag{B2}$$

where a, b and c denote the length, width and height of the rectangular cell, respectively.

References

Badea, E.A., Everett, M.E., Newman, G.A., Biro, O., 2001. Finite-element analysis of controlled-source electromagnetic induction using Coulomb-gauged potentials. Geophysics 66 (3), 786–799.

Ben, F., 2016. 3D Marine Controlled-source Electromagnetic Modeling and Inversion Theory and Research on the Mechanism of Anisotropic Effect. Ph.D. Thesis. Jilin University.

Bíró, Oszkár, 1999. Edge element formulations of eddy current problems. Comput. Methods Appl. Mech. Eng. 169 (3–4), 391–405.

Cai, H., 2015. Three-dimensional marine controlled-source electromagnetic modelling in anisotropic medium using finite element method. Chin. J. Geophys. 58 (6), 2839–2850.

Cai, H., Xiong, B., Han, M., Zhdanov, M., 2014. 3D controlled-source electromagnetic modeling in anisotropic medium using edge-based finite element method. Comput. Geosci. 73, 164–176.

Cao, H., Wang, K., Wang, T., Hua, B., 2018. Three-dimensional magnetotelluri axial anisotropic forward modeling and inversion. J. Appl. Geophys. 153, 75–89.

Chen, H.B., Li, T.L., Xiong, B., 2017. Finite-element modeling of 3D MCSEM in arbitrarily anisotropic medium using potentials on unstructured grids. Chin. J. Geophys. 60 (6), 698–709.

Dekker, D.L., Hastie, L.M., 1980. Magneto-telluric impedances of an anisotropic layered Earth model. Geophys. J. Int. 61 (1), 11–20.

Everett, M.E., 2012. Theoretical developments in electromagnetic induction geophysics with selected applications in the near surface. Surv. Geophys. 33 (1), 29–63.

Haber, E., Ascher, U.M., Aruliah, D.A., Oldenburg, D.W., 2000. Fast simulation of 3D electromagnetic problems using potentials. J. Comput. Phys. 163 (1), 150–171.

Han, B., Li, Y., Li, G., 2018. 3-D forward modeling of magnetotelluric fields in general anisotropic media and its numerical implementation in Julia. Geophysics 83 (4), 1–45.

Häuserer, M., Junge, A., 2011. Electrical mantle anisotropy and crustal conductor: a 3-D conductivity model of the Rwenzori Region in western Uganda. Geophys. J. Int. 185 (3), 1235–1242.

Hu X. Y., Huo G. P., Gao R., & Wang H Y. 2013. The magnetotelluric anisotropic two-dimensional simulation and case analysis. Chin. J. Geophys., 56(12):4268:4277.

Jin, J.M., 2002. The Finite Element Method in Electromagnetics. 2nd ed. John Wiley and Sons, New York.

Jones, A.G., 2012. Distortion decomposition of the magnetotelluric impedance tensors from a one-dimensional anisotropic Earth. Geophys. J. Int. 189 (1), 268–284.

Koldan, J., Puzyrev, V., de la Puente, J., Houzeaux, G., Cela, J.M., 2014. Algebraic multigrid preconditioning within parallel finite-element solvers for 3-D electromagnetic modelling problems in geophysics. Geophys. J. Int. 197 (3), 1442–1458.

Kong, W., Lin, C., Tan, H., Peng, M., Tong, T., Wang, M., 2018. The effects of 3D electrical anisotropy on magnetotelluric responses: synthetic case studies. J. Environ. Eng. Geophys. 23 (1), 61–75.

Li, Y., 2000. Finite Element Modeling of Electromagnetic Fields in Two- and Three-dimensional Anisotropic Conductivity Structures. Ph.D. Thesis. University of Gottingen.

Li, Y., 2002. A finite-element algorithm for electromagnetic induction in two-dimensional anisotropic conductivity structures. Geophys. J. Int. 148 (3), 389–401.

Li, Y., Pek, J., 2008. Adaptive finite element modelling of two-dimensional magnetotelluric fields in general anisotropic media. Geophys. J. Int. 175 (3), 942–954.

Li, J., Farquharson, C.G., Hu, X., 2016. 3D vector finite-element electromagnetic forward modeling for large loop sources using a total-field algorithm and unstructured tetrahedral grids. Geophysics 82 (1), E1–E16.

Linde, N., Pedersen, L.B., 2004. Evidence of electrical anisotropy in limestone formations using the RMT technique. Geophysics 69 (4), 909–916.

Liu, Y.H., Yin, C.C., Ren, X.Y., Qiu, C.K., 2016. 3D parallel inversion of time-domain airborne EM data. Appl. Geophys. 13 (4), 701–711.

Liu, Y., Xu, Z., Li, Y., 2018. Adaptive finite element modelling of three-dimensional magnetotelluric fields in general anisotropic media. J. Appl. Geophys. 151, 113–124.

Mitsuhata, Y., Uchida, T., 2004. 3D magnetotelluric modeling using the T-Ω finite-element method. Geophysics 69 (1), 108–119.

O'Brien, D.P., Morrison, H.F., 1967. Electromagnetic fields in an n-layer anisotropic half-space. Geophysics 32 (4), 668–677.

Pek, J., Santos, F.A., 2002. Magnetotelluric impedances and parametric sensitivities for 1-D anisotropic layered media. Comput. Geosci. 28 (8), 939–950.

Pek, J., Verner, T., 1997. Finite-difference modelling of magnetotelluric fields in two-dimensional anisotropic media. Geophys. J. Int. 128 (3), 505–521.

Puzyrev, V., Koldan, J., de la Puente, J., Houzeaux, G., Vázquez, M., Cela, J.M., 2013. A parallel finite-element method for three-dimensional controlled-source electromagnetic forward modelling. Geophys. J. Int. 193 (2), 678–693.

Reddy, I.K., Rankin, D., 1971. Magnetotelluric effect of dipping anisotropies. Geophys. Prospect. 19 (1), 84–97.

Ren, Z., Kalscheuer, T., Greenhalgh, S., Maurer, H., 2013. A goal-oriented adaptive finite-element approach for plane wave 3-D electromagnetic modelling. Geophys. J. Int. 194 (2), 700–718.

Tan, H.D., Yu, Q.F., Booker, J., Wei, W., 2003. Magnetotelluric three-dimensional modeling using the staggered-grid finite difference method. Chin. J. Geophys. 46 (5), 705–711.

Wang, K., Tan, H., Zhang, Z., Li, Z., Cao, M., 2016. Divergence correction schemes in finite difference method for 3D tensor CSAMT in axial anisotropic media. Explor. Geophys. 48 (4), 363–373.

Weidelt, P., Oristaglio, M., Spies, B., 1999. 3-D Conductivity Models: Implications of Electrical Anisotropy. Three-dimensional electromagnetics. Vol. 7 pp. 119–137.

Xiao, T., Liu, Y., Wang, Y., Fu, L.Y., 2018. Three-dimensional magnetotelluric modeling in anisotropic media using edge-based finite element method. J. Appl. Geophys. 149 (1–9).

Xu, S.Z., 1994. The Finite Element Methods in Geophysics. Science Press, Beijing, China.

Xue, B., Ji, Y., 2018. Generalized analytic solutions and response characteristics of magnetotelluric fields on anisotropic infinite faults. J. Geophys. Eng. 15 (3), 962.

Yin, C., 2000. Geoelectrical inversion for a one-dimensional anisotropic model and inherent non-uniqueness. Geophys. J. Int. 140 (1), 11–23.

Yin, C., 2003. Inherent nonuniqueness in magnetotelluric inversion for 1D anisotropic models. Geophysics 68 (1), 138–146.